Deimos: An Obstacle to the Solar Wind

K. Sauer, E. Dubinin, K. Baumgärtel, A. Bogdanov

Two isolated solar wind disturbances about 5 minutes in duration were detected aboard the Russian spacecraft Phobos-2 upon its crossing the wake of the martian moon Deimos about 15,000 kilometers downstream from the moon on 1 February 1989. These plasma and magnetic events are interpreted as the inbound and outbound crossings of a Mach cone that is formed as a result of an effective interaction of the solar wind with Deimos. Possible mechanisms such as remanent magnetization, cometary type interaction caused by heavy ion or charged dust production, and unipolar induction resulting from the finite conductivity of the body are discussed. Although none of the present models is fully satisfactory, neutral gas emission through water loss by Deimos at a rate of about 10^{23} molecules per second, combined with a charged dust coma, is favored.

During its first elliptical orbits around Mars in February 1989, the Russian Phobos-2 spacecraft observed several isolated magnetic disturbances outside of the martian bow shock. Such events were detected, for example, at the crossing points of the spacecraft with the orbit of the martian moon Phobos. One of the events, however, occurred between the orbits of Phobos and Deimos (called "mysterious event"). The events (referred to here as E1 and E2) are seen as isolated perturbations in the magnitude of the interplanetary magnetic field (IMF) (Fig. 1). These perturbations are accompanied by variations of the electron number density, which was detected by the electric probe. An interpretation has been attempted hitherto only for the events near the orbit of the moon Phobos. A ring of charged dust particles along the orbit of Phobos has been suggested as the source of the perturbations. Indeed, a cloud of charged dust interacts effectively with the solar wind even if its peak charge density is lower than that of the solar wind (*1*). The perturbations are carried by magnetosonic or whistler waves, which may produce upstream phenomena as a result of their large group velocity along the undisturbed magnetic field. The existence of a gaseous torus along the orbit of Phobos as a result of collisional accretion of exospheric oxygen atoms and dust particles was also discussed as a possible source of disturbances (*2, 3*). However, this hypothesized torus is too weak to produce strong variations in the density of the solar wind plasma ($\Delta n \sim n$) and in the magnetic field ($\Delta B \sim B$). Moreover, all of these models left without answer the question about the origin of the "mysterious" event that is located between the orbits of the martian moons.

We suggest that both events are caused by the outer martian moon, Deimos, which was in a favorable position relative to the spacecraft during the time interval between events E1 and E2 (E2 is probably a result of a combined action of both Deimos and the Phobos dust torus) (Fig. 2A). The distance between the spacecraft and Deimos was about 15,000 km. The position of the spacecraft relative to Deimos suggests that E1 and E2 are intersection points of the spacecraft orbit with a Mach cone emanating from Deimos. The magnetosonic Mach number $M_{AS} = V_{sw}/(V_A{}^2 + V_s{}^2)^{1/2}$, where V_{sw}, V_A, and V_s, are the solar wind velocity, the Alfvén velocity, and the ion acoustic velocity, was about 9, which corresponds to an opening angle for the Mach cone of about 13°. Anisotropic properties of wave propagation in a magnetized plasma could produce an asymmetry of the Mach cone. However, the surface of group velocities of the fast magnetosonic waves is close to spherical [$V_{AS} = (V_A{}^2 + V_s{}^2)^{1/2} \sim 85$ km/s, $V_S \sim 70$ km/s] and any asymmetry of the Mach cone is expected to be small. Because the satellite moves faster than Deimos by about 1 km/s, it crossed the cone twice, inbound and outbound. The diameter of the cone along the spacecraft orbit is about 4000 km. Assuming that the spacecraft traversed a spatial structure, the extent of the events is about 300 to 500 km (Fig. 2B).

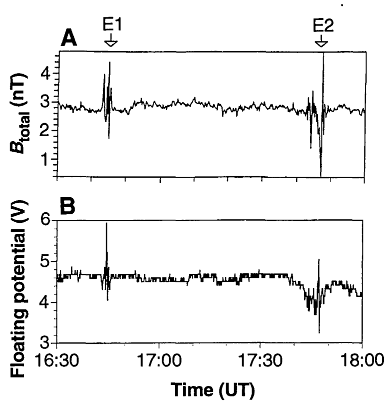

Fig. 1. (**A**) Variation of the magnitude of the magnetic field during the first approach of the Phobos-2 spacecraft to Mars on 1 February 1989. Two isolated magnetic disturbances at 16:45 and 17:45 UT are labeled as E1 and E2. (**B**) Variations of the floating potential V_{fl}, which is a good indicator of variations in the electron number density (variations of V_{fl} and n_e are anticorrelated).

Bogdanov (*4*) had already pointed out an efficient interaction between Deimos and the solar wind after the Mars mission of 1976. The conclusions were based on a relative position of the spacecraft and Deimos similar to that shown in Fig. 2 and a significant decrease of the proton density accompanied by a temperature increase for a duration of 30 min. The corresponding magnetic field data were not helpful because the sensitivity of the magnetometer was too low. The author concluded that Deimos behaves as a weak comet, producing a downstream proton rarefaction region. A causal relation between the plasma and magnetic field structures observed by Phobos-2 near 17:20 UT and the upstream position of Deimos was already suggested in (*5*), but no connection was seen to the adjacent, more pronounced events E1 and E2.

There are several mechanisms that could explain how a small body such as Deimos could perturb the solar wind (*6*): cometary outgassing, remnant magnetization, unipolar induction, or a charged dust sphere around the body. A comet-type obstacle remains one of the most effective sources of perturbations in the solar wind, and Deimos acting as a source for charged heavy particles by either outgassing like a weak comet or by dust emission and the subsequent processes cannot be ruled out.

Two-dimensional fluid simulations of the solar wind interaction with different types of obstacles were carried out. The protons (p) and heavy ions (h) were considered as separate fluids coupled by electromagnetic forces. In a first step, however, it is sufficient to investigate the solar wind response to an immobile heavy ion cloud (HIC) of a prescribed density profile. The model system of equations follows from the full set of bi-ion fluid equations (*7*) by assuming that the heavy ions are immobile (mass $m_h \rightarrow \infty$). Thus, the interaction of the solar wind with a HIC is described by the continuity and momentum equations for the protons

$$\frac{\partial}{\partial t} n_p + \nabla \cdot (n_p \mathbf{v}_p) = 0 \qquad (1)$$

$$\frac{\partial}{\partial t}(n_p \mathbf{v}_p) + \nabla \cdot n_p \mathbf{v}_p \mathbf{v}_p = \frac{1}{m_p}\frac{n_p}{n_e} \left\{ e n_h \mathbf{v}_p \times \mathbf{B} - \nabla\left[\left(p_e + \frac{B^2}{2\mu_0}\right)\mathbf{I} - \frac{\mathbf{BB}}{\mu_0}\right]\right\} \qquad (2)$$

K. Sauer, K. Baumgärtel, A. Bogdanov, Max-Planck-Institut für extraterrestrische Physik, Außenstelle, Rudower Chausse 5, 12489, Berlin, Germany.
E. Dubinin, Space Research Institute, Profsojuznaja Street 84/32, 117810 Moscow, Russia.

and Faraday's law

$$\frac{\partial}{\partial t}\mathbf{B} - \nabla \times \left[\frac{1}{n_e}\left(n_p \mathbf{v}_p - \frac{1}{\mu_0}\nabla \times \mathbf{B}\right) \times \mathbf{B}\right] = 0 \quad (3)$$

where n_x is the number density of particle x, $\mathbf{v}_p$ is the proton velocity, $\mathbf{B}$ is the magnetic field, and μ_0 is the permeability of free space; the electron density n_e is obtained from the quasi-neutrality condition $n_e = n_p + n_h$ and the electron pressure $p_e = n_e k T_e$ (k, Boltzmann's constant) is calculated for isothermal conditions (electron temperature T_e = constant). The HIC (charged dust or molecules) enters the equations only in the charge density n_h, whose spatial profile is prescribed. Equations 1 through 3 were solved numerically applying the flux-corrected transport scheme of Boris and Book (8). The parameters of the inflowing solar wind were fixed at the left-hand boundary. The magnetic field was assumed to be in the simulation plane transverse to the flow. Figure 3 presents results of the simulation run. A well-developed Mach cone at distances of about $100L$ (length $L = c/\Omega_{pi} \approx 160$ km, where c is the speed of light and Ω_{pi} is the proton plasma frequency) appears only if the peak charge density of the ion cloud becomes comparable with the proton number density in the plasma flow.

Figure 4A shows variations of the plasma parameters through the tail in the simulation run at a distance $x/L = 100$, which corresponds to 15,000 km in the martian environment. For comparison, Fig. 4B shows the variations of the solar wind plasma measured by the ASPERA (Automatic Space Plasma Experiment with a Rotating Analyser) spectrometer and the PWS (Plasma Wave System) probe system. The Phobos-2 spacecraft approaching the planet along the elliptical orbit was in the spinning mode. This affected plasma measurements made by the ion and electron spectrometers. The effects caused by the spinning were mostly displayed in plasma density data; bulk velocity measurements were less sensitive to the imperfect stabilization of the spacecraft, and measurements of the electron number density made by the electric probe were not sensitive to the spacecraft rotation. Parameters of the solar wind taken from the ASPERA spectrometer data were $n = 2$ cm^{-3}, $V = 770$ km/s, ion temperature $T_i \approx 13$ eV; and $T_e \approx 15$ eV; the magnetic field value was 3 nT. The smoothing procedure used to eliminate effects of the spacecraft spinning in the ASPERA data results in some "spreading" of the events. A reasonable agreement of the data with the simulations is seen. Asymmetry of disturbances between inbound and outbound events that is not observed in the simulation run arises probably as a result of the solar wind flow component of the IMF and the action of the Phobos dust torus.

If the Mach cone is formed by a HIC, there must be a source of charged particles around Deimos capable of producing a sufficiently high charge number density (comparable to the solar wind density). One possible source is the production of heavy ions by outgassing. It is assumed that the martian moons contained a significant amount of water in their interiors and have not lost it over geological time. According to (9), the present water flux may reach values of $\sim 10^{23}$ s^{-1}. After photoionization, ions are picked up by the solar wind. It can be estimated, by evaluating the balance of newly produced particles and those carried away by the solar wind, that a production rate of about 10^{23} s^{-1} is sufficient to maintain an equilibrium ion water distribution with a peak density comparable with the number density of the solar wind protons and a characteristic dimension of about $2L$. Simulations of the ion distribution near Deimos confirm this. Therefore, loss of the water by Deimos may be the reason for its effective interaction with the solar wind.

An additional source of heavy charged particles around Deimos could be the production of dust particles as the result of intermittent meteoroid bombardment of its surface. The ejected dust grains are affected

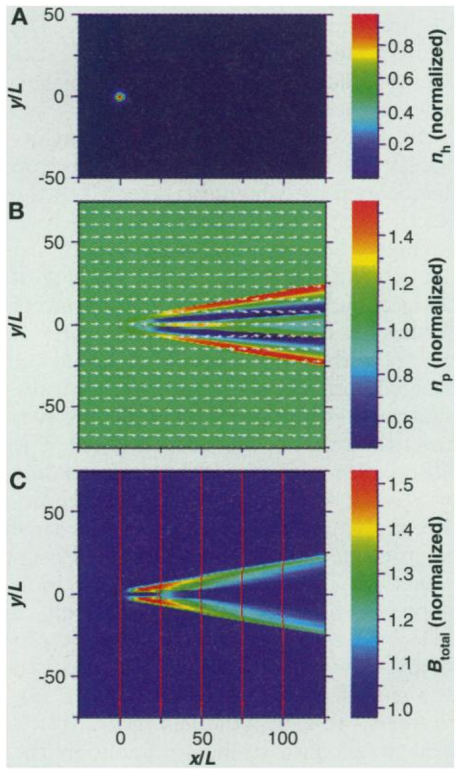

Fig. 3. Formation of a Mach cone owing to the interaction of the solar wind with an immobile ion cloud. (**A**) Two-dimensional distribution of the charged "dust" density with an extension of about 300 km. The spatial structures of (**B**) the proton density (n_p) and (**C**) the magnetic field (B_{total}) illustrate the formation of a Mach cone. White arrows in (B) correspond to flow velocity vectors. Red curves in (C) are magnetic field lines. The plasma parameters are normalized with their corresponding undisturbed values; x and y are given in units of the proton inertial length $L = c/\Omega_{pi}$ $\approx$ 160 km.

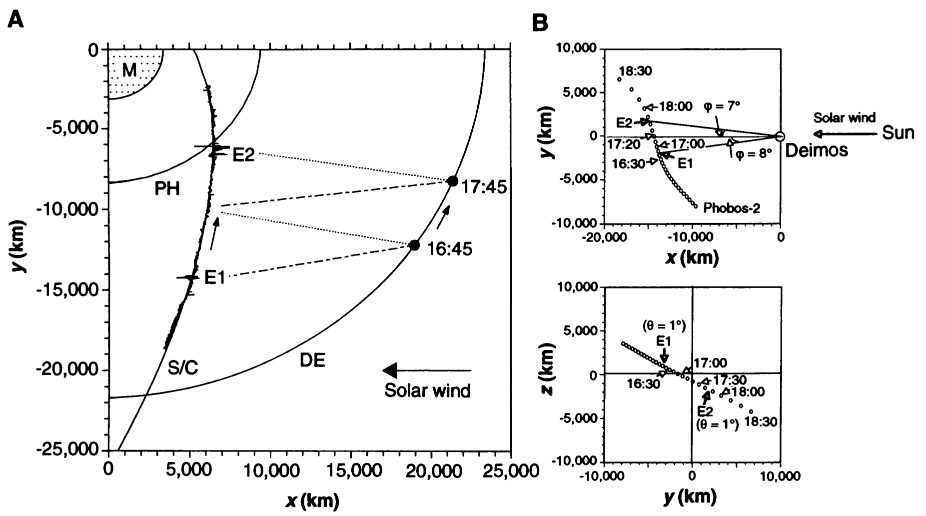

Fig. 2. (**A**) Location of the magnetic events E1 and E2 (1 February 1989) in relation to the motion of Deimos. The spacecraft (S/C) trajectory and the orbits of the martian moons Phobos (PH) and Deimos (DE) are plotted as solid lines. The curve along the spacecraft trajectory represents the relative deviation of the magnetic field magnitude from its mean value over 3 hours (resolution of 10 s). The dotted and dashed-dotted lines illustrate that E1 and E2 may be related to spacecraft crossings of the left and right borders, respectively, of a Mach cone formed by the solar wind–Deimos interaction. (**B**) The geometry of mutual positions of the spacecraft and the martian moon in the Deimos reference frame: x points to the sun, y opposes planetary motion of Mars, and z completes the right-hand set. The angles φ and θ show the angular positions of the events in xy and xz plane.

by different forces (radiation pressure, gravity, and electromagnetic forces). Depending on their masses, some of the grains survive in the dust rings, whereas other particles form a dust halo around Mars (*10*). None of the existing models considers the distribution of dust particles in the vicinity of the martian moons. There were only efforts to simulate dust tori along the orbits of Deimos and Phobos. Different models give a rather wide range of values of n_{dust} in the dust tori of the martian moons. According to (*2*), the number density of 100-μm particles in the narrow (~400 km) belt along the orbit of Phobos is about 10^{-7} cm^{-3} and the charge density $qn_{\text{dust}} \sim 0.2$ electron per cubic centimeter, or ~10% of the proton charge density for the analyzed time interval. Other models (*10*) predict much lower values for the number density of dust particles that occupy a very large volume around Mars. Indirect evidence of dusty particles near the martian moons was reported in (*11*). Our conclusion, however, is that the continuous formation of a dust coma around Deimos with charge densities similar to the solar wind density seems to be not very likely. Therefore, dust production can only be treated as an additional particle source to possible water emission of Deimos.

Remnant magnetization is another possibility for a small body to disturb the solar wind flow. Observations by the Galileo satellite at its encounters with the asteroids Gaspra (*12*) and Ida (*13*) together with Hall-Magnetohydrodynamic simulations (*13, 14*) strongly favor an explanation in terms of solar wind interaction with a magnetic dipole. Even for moderate magnetic moments, perturbations in the whistler mode are created and transported in a direction guided by the undisturbed magnetic field.

On the basis of spectral optical measurements and comparison with meteorites, Deimos is believed to be of carbonaceous chondrite composition. The magnetization of carbonaceous chondrites estimated from that of meteoritic material corresponds to a surface magnetic field of 100 to 1000 nT (*6*). Such field values can not only strongly deflect the solar wind but can even create a peculiar minimagnetosphere. The effective size of the obstacle, several tens of kilometers, remains below the proton skin depth, and so most of the disturbances are transported as whistler waves (*15*), similar to those seen at Gaspra. Only for surface fields between 10^4 and 10^5 nT, which are the highest reasonable values found in the literature for chondrites (*16*), could the effective size of the obstacle exceed the critical value of about 100 km. Thus, the possibility of Deimos being a strongly magnetized body cannot be ruled out totally.

Solar wind perturbations can also be generated by unipolar induction if the small body or at least its crust is electrically conducting. This has been studied both experimentally and theoretically (*17*). The carbonaceous chondrites have a rather high electrical conductivity and can form an efficient unipolar dynamo in the solar wind plasma. Deimos may generate disturbances in the solar wind if electrical currents flow through its interior and close in the ambient plasma. The dimensionless parameter that characterizes the "efficiency" of the obstacle to the solar wind flow is the magnetic Reynolds number $Re_{\text{m}} = \mu_{\text{o}}\sigma V_{\text{sw}} d$, where σ is the electrical conductivity of the body and d is the diameter of the obstacle. Electrical conductivity of carbonaceous chondrites reaches 10^{-2} S/m, even at low surface temperatures (*18*). This gives $Re_{\text{m}} \approx 60 \gg 1$. However, closing currents in the solar wind plasma cannot support such large current densities ($j = \sigma V_{\text{sw}} B \sim 10^{-5}$ A/m^2) in the body. This may lead to an essential limitation of the unipolar current (*6*). The limiting current density in the solar wind plasma carried by electrons ($j_{\text{lim}} \sim n_{\text{e}} e V_{\text{the}}$, where V_{the} is the thermal electron velocity) is about $(5 \div 8) \times 10^{-7}$ A/m^2. This limitation of the neutralization of the excess charge by plasma currents may result in the polarization of Deimos and the attenuation of perturbations. In this case, the effective diameter of the obstacle is also small, although the possible existence of a dense ion cloud around Deimos with a large number of the current carriers can increase this scale.

The relatively large grid size ($\Delta x = 0.75L$) used in Fig. 3 was not sufficient to resolve fine structures within the Mach cone that may be caused by whistler waves. To test this effect, we performed a simulation with a smaller box ($L_x = L_y = 20L$, $\Delta x = 0.1L$). Figure 5A shows variations of the magnetic field value and the proton number density. A fine structure of the Mach cone appears. Figure 5B gives E1 at the high resolution. The event consists of compressional and rarefactional disturbances, supporting the notion that they are on the magnetoacoustic branch. There is a correlation between variations of the magnetic field and electron number density ($\delta n \sim \delta B$). The structure of E2 is more complicated: "splitting" of the wave is observed. This might be caused by the superposition of waves resulting from the combined action of both Deimos and the Phobos dust torus, as well as by

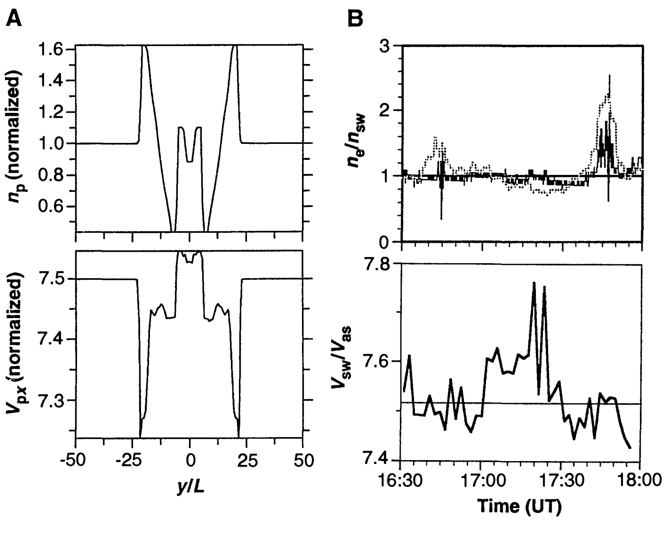

Fig. 4. (**A**) Variations of the plasma parameters through the tail in the simulation run at the $x/L = 100$, which is approximately scaled to the distance where the Phobos-2 spacecraft crossed the Deimos wake. (**B**) For comparison, variations of the solar wind plasma measured by the ASPERA and the PWS instruments are given. Some difference in the structure of the events recorded by the different instruments is caused by the smoothing procedure of the ASPERA data (dotted line in n_e/n_{sw}) used to eliminate effects of an imperfect stabilization of the spacecraft.

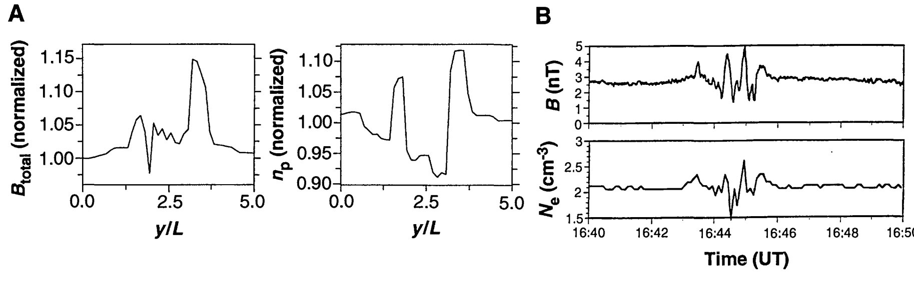

Fig. 5. (**A**) The structure of the Mach cone in the simulation run with a smaller grid size ($\Delta x = 0.1L$). (**B**) The event E1 in high resolution is shown for comparison. Strong variations of the plasma number density indicate that perturbations are on the magnetoacoustic branch.

the nonlinear evolution of a kinetic magnetosonic wave (*19*).

We conclude that there is presently no clearly dominant mechanism that makes Deimos such an effective obstacle to the solar wind, although the idea of a charged ion cloud around Deimos is favored. Future international space missions to Mars (Mars-96, Mars-Observer, Planet-B) will certainly improve our knowledge about the plasma-dust environment of the martian moons. Three-dimensional simulations of the dynamical response of a magnetoplasma to small celestial bodies are also necessary. This modeling could be used as a tool for remote sensing of physical properties of the martian moons and asteroids.

REFERENCES AND NOTES

1. K. Baumgärtel and K. Sauer, *Ann. Geophysicae* **10**, 763 (1992); K. Sauer *et al.*, *Geophys. Res. Lett.* **20**, 165 (1993); U. Motschmann *et al.*, *ibid.*, **19**, 225 (1992); K. Baumgärtel and K. Sauer, *Adv. Space Res.* **13**, 291 (1993).
2. W.-H. Ip and K. Banaszkiewicz, *Geophys. Res. Lett.* **17**, 857 (1990).
3. E. M. Dubinin *et al.*, *ibid.*, p. 861.
4. A. V. Bogdanov, *J. Geophys. Res.* **86**, 6926 (1981).
5. E. M. Dubinin *et al.*, *Planet. Space Sci.* **39**, 123 (1991).
6. F. Herbert, *Adv. Space Res.* **13**, 249 (1993).
7. K. Sauer *et al.*, *Geophys. Res. Lett.* **21**, 2255 (1994).
8. D. L. Book *et al.*, in *Finite-Difference Techniques for Vectorized Fluid Dynamics Calculations*, D. L. Book, Ed. (Springer, New York, 1981), p. 29.
9. F. P. Fanale and J. R. Salvail, *Geophys. Res. Lett.* **16**, 287 (1989).
10. M. Horanyi *et al.*, *ibid.* **17**, 853 (1990); A. Juhasz *et al.*, *J. Geophys. Res.* **98**, 1205 (1993); H. Ishimoto and T. Mukai, *Planet. Space Sci.* **42**, 691 (1994).
11. E. Dubinin, *Adv. Space Res.* **13**, 10271 (1993).
12. M. Kivelson *et al.*, *Science* **261**, 331 (1993).
13. M. Kivelson *et al.*, *Adv. Space Res.* **16**, 459 (1995).
14. K. Baumgärtel, K. Sauer, A. Bogdanov, *Science* **263**, 653 (1994).
15. C. K. Goertz, *Planet. Space Sci.* **32**, 1387 (1984); R. Stenzel, J. Urrutia, C. Rousculp, *Phys. Fluids B* **5**, 325 (1993).
16. M. Terho *et al.*, in *Abstracts for "Small Bodies in the Solar System and their Interaction with the Planets,"* H. Rickman and M. Dahlgren, Eds. (Mariehamn, Åland, Finland, 1994), p.159.
17. L. J. Srnka , in *Proton and Particle Interactions with Surfaces in Space*, R. J. Grard, Ed. (Reidel, Boston, 1973), p. 481; A. Barnett and S. Olbert, *J. Geophys. Res.* **91**, 10117 (1986).
18. W.-H. Ip and F. Herbert, *Moon Planets* **28**, 43 (1983).
19. N. Omidi and D. Winske, *J. Geophys. Res.* **95**, 2281 (1990).

20. We are grateful to the FGMM team, and also K. Schwingenschuh and R. Grard for providing of magnetometers and the probe data. The work was done while E.D. visited Max-Planck-Institut für extraterrestrische Physik, which he thanks for their financial support and hospitality in Berlin.

6 March 1995; accepted 6 July 1995

Photodeposition of Micrometer-Scale Polymer Patterns on Optical Imaging Fibers

Brian G. Healey, Stacy E. Foran, David R. Walt*

Microstructures were fabricated on optical imaging fibers with a photopolymerization technique. Monodisperse polymeric microarrays were produced containing spots of 2.5 micrometers in diameter spaced 4.5 micrometers apart. Polymer microarrays were also deposited on other substrates by using imaging fibers for light delivery. The technique allows micrometer-scale photopatterning with masks larger than the desired dimensions.

There has been considerable interest in preparing micrometer- and nanometer-scale structures such as nanotubes (*1*), nanowires (*2*), quantum dots (*3*), microspheres (*4*), and nanometer-size light-emitting diodes (*5*). Complex, well-defined microstructures have been produced by techniques including laser-assisted chemical vapor deposition (*6*) and the creation of hydrophobic templates from photoresists for the deposition of self-assembled monolayers on gold (*7*). Photoactivation techniques have also been used to fabricate well-defined microstructures; for example, photolithography has been used for information storage in photoconductive materials (*8*), photoassembly of combinatorial libraries (*9*), and site-selective covalent attachment of biomolecules (*10*). Here we report a simple technique for the fabrication of patterned microstructures. Specifically, we use the discrete light pathways in an optical imaging fiber to photopolymerize an array of individual polymer spots in a variety of sizes and patterns.

Optical imaging fibers are hexagonally packed bundles of individual fibers melted and drawn together so as to maintain the same relative position for each fiber in the bundle throughout its length (*11*). Such bundles can carry coherent images from one end of the bundle to the other and have been used extensively for medical imaging. The present technique is based on chemistry developed in our laboratory for preparing fiber-optic sensors (*12*). The distal end of an imaging fiber is first functionalized by treatment with 3-trimethoxysilylpropylmethacrylate to attach a photopolymerizable acrylate group to the glass surface which facilitates the adhesion of the polymer to the glass surface. The fiber is then placed on the photodeposition system (Fig. 1A). Collimated light from a mercury-xenon arc lamp is passed through a neutral density filter slide and then through an excitation bandpass filter to isolate the appropriate initiation light. The initiation light passes through a mask and is imaged onto the proximal end of the fiber (Fig. 1B). The distal end of the fiber is then coated with a thin film of prepolymer by dipping it in a small volume of solution containing photoinitiator, solvent, and a monomer or oligomer that can be photocrosslinked (*13*). The fiber is then illuminated for a fixed time by an electronic shutter (*14*), and the excess polymerization solution is removed by rinsing with ethanol.

First we produced microstructures by using a pinhole mask and placing a focusing lens between the excitation filter and the pinhole (Fig. 2, A and B). A 25-μm-diameter spot was imaged onto the fiber. Polymer formed only on the individual fiber cores because the glass claddings between the fibers of the bundle do not propagate light. In Fig. 2A, the hexagonal packing of the 2- to 3-μm-diameter polymer spots is seen clearly with a spacing between spots (center to center) of 4 to 5 μm. This pattern corresponds identically to the individual pixels of the imaging fiber. The side view of the pattern shows that the polymer spots are approximately 2 to 3 μm in height and appear as hemispheres on the fiber surface (Fig. 2B). The polydispersity of the polymer microspots is due to the gaussian distribution of light exiting the pinhole and the type of imaging fiber used. Polymer spots on the edges are smaller as a result of decreased light intensity, and the noncircular polymer spots (Fig. 2A, top view) are a result of nonuniform fibers in the bundle. Monodisperse polymeric microstructures were fabricated with a defect-free imaging fiber (Fig. 2C) and had polymer spots 2.5 μm in diameter, spaced 4.5 μm apart, and 1.2 μm high (*15*).

On careful examination of a scanning electron micrograph (SEM) from a different polymer array preparation, we observed that triangular wells with 1-μm edges could be produced by controlling the polymerization reaction composition and time carefully (Fig. 2D). The wells were fabricated by increasing the concentration of photocross-linkable oligomer and increasing the illumination time. During polymerization, the polymer first deposits on the fiber cores and then continues to deposit between the fibers where the cores have their closest approach. The polymer wall between the wells is less than 0.5 μm wide and 1.0 μm high. The triangular wells have a volume of 460 al (1 al

Max Tishler Laboratory for Organic Chemistry, Department of Chemistry, Tufts University, Medford, MA 02155, USA.

*To whom correspondence should be addressed.